

Reconstruction and performance evaluation of FASER's emulsion detector at the LHC



The FASER collaboration

Roshan Mammen Abraham et al.

Full author list at the end of the paper

E-mail: faser-publications@cern.ch

ABSTRACT. This paper presents the reconstruction and performance evaluation of the FASER ν emulsion detector, which aims to measure interactions from neutrinos produced in the forward direction of proton-proton collisions at the CERN Large Hadron Collider. The detector, composed of tungsten plates interleaved with emulsion films, records charged particles with sub-micron precision. A key challenge arises from the extremely high track density environment, reaching $O(10^5)$ tracks per cm^2 . To address this, dedicated alignment techniques and track reconstruction algorithms have been developed, building on techniques from previous experiments and introducing further optimizations. The performance of the detector is studied by evaluating the single-film efficiency, position and angular resolution, and the impact parameter distribution of reconstructed vertices. The results demonstrate that an alignment precision of $0.3 \mu\text{m}$ and robust track and vertex reconstruction are achieved, enabling accurate neutrino measurements in the TeV energy range.

KEYWORDS: Data processing methods; Detector alignment and calibration methods (lasers, sources, particle-beams); Particle tracking detectors; Performance of High Energy Physics Detectors

ARXIV EPRINT: [2504.13008](https://arxiv.org/abs/2504.13008)



Contents

1	Introduction	1
2	The emulsion detector	2
3	Reconstruction	4
3.1	Base-track formation	4
3.2	Alignment	6
3.3	Track reconstruction	7
3.4	Vertex reconstruction	8
3.5	Track follow-down	8
4	Evaluation of detector performance	9
4.1	Track density	10
4.2	Single-film efficiency	10
4.3	Position and angular resolution	10
4.4	Impact parameter	13
5	Conclusion	14
	The FASER collaboration	17

1 Introduction

One of the primary physics goals of the ForwArd Search ExpeRiment (FASER) [1–4] at CERN’s Large Hadron Collider (LHC) [5] is to study neutrinos produced in the forward direction of the LHC proton-proton (pp) collisions, with energies in the TeV range [6, 7]. In 2021, the FASER Collaboration reported the first evidence of neutrino interaction candidates produced at the LHC [8]. In 2023, the first observation of collider muon neutrinos was achieved using FASER’s electronic detector components [9]. Subsequently, the FASER Collaboration reported the first measurement of the muon neutrino interaction cross section and flux as a function of energy [10]. The interactions of all three neutrino flavours can be measured by identifying leptons generated through neutrino charged-current (CC) interactions with the FASER ν emulsion detector [4]. For the first time, FASER measured ν_e and ν_μ interaction cross sections using a 128 kg subset of the FASER ν detector after exposure to 9.5 fb^{-1} of 13.6 TeV pp collisions [11]. Charged particle tracks are reconstructed with sub-micron precision, enabling the measurement of the energy of the electrons and the momentum of the charged particles, including muons.

The FASER ν detector is placed 480 meters downstream from the ATLAS interaction point (IP1), aligned with the collision axis line of sight (LOS). Many of the charged particles from the LHC collisions are deflected by the LHC magnets, while neutral hadrons are absorbed by the approximately 100 meters of rock in front of the detector. However, given the 40 MHz collision rate at the LHC, many charged particles, such as muons, still reach the FASER ν emulsion detector. It is therefore

unavoidable to accumulate a large number of charged particle tracks, which poses a challenge for track and vertex reconstruction from neutrino interactions.

The identification of track segments from fully automated emulsion film scanning systems was initially performed by means of the NETSCAN software [12], originally developed for the DONuT experiment [13] and later adapted for the CHORUS experiment [14]. The FEDRA emulsion reconstruction framework [15] and NETSCAN 2.0 [16] were subsequently developed for the OPERA experiment. These tools incorporated film-to-film alignment, track reconstruction, topological decay search, momentum measurement, and electromagnetic shower reconstruction. A comprehensive historical overview of nuclear emulsion technologies and their development is presented in ref. [17].

Recent experiments, such as NA65/DsTau [18] and FASER, present new challenges, requiring the reconstruction of data in a high track density environment ($\mathcal{O}(10^5) - \mathcal{O}(10^6)$ tracks per cm^2), approximately three orders of magnitude higher than OPERA's track density of 100–1000 tracks per cm^2 . Dedicated reconstruction algorithms to address these challenges were initially developed for DsTau [18]. The reconstruction of the FASER data builds on the FEDRA framework and DsTau algorithms, incorporating further optimizations to suit the specific conditions of FASER. Alignment techniques were also developed to fully exploit the high spatial resolution of the emulsion detector.

This paper describes the reconstruction techniques developed for FASER ν and the performance evaluation of the emulsion detector. Section 2 presents the detector, the temperature monitoring during exposure, and the automated scanning system. Section 3 describes the reconstruction process, which includes alignment techniques, track reconstruction, and vertex reconstruction. Section 4 discusses the performance evaluation of the emulsion detector based on the reconstructed tracks.

2 The emulsion detector

Figure 1 shows a schematic of the FASER ν emulsion detector.¹ The emulsion detector has a transverse size of $25\text{ cm} \times 30\text{ cm}$ and a length of approximately 100 cm. The total mass of the detector is approximately 1.1 t, corresponding to 220 radiation lengths along the beam. It consists of a repeated structure of 730 layers, each composed of a tungsten plate with a thickness of 1.1 mm and an emulsion film. The film is made by coating both sides of a transparent polystyrene base with a gel consisting of silver bromide crystals embedded in gelatin [17]. The film consists of two emulsion layers, each $65\ \mu\text{m}$ thick, deposited on both sides of the $210\ \mu\text{m}$ thick base.

The emulsion gel and the films were produced at the large-scale facility of Nagoya University [19]. In order to enhance sensitivity and reduce background, the films were exposed to high-humidity conditions, 95% R.H. (Relative Humidity), at $30\text{ }^\circ\text{C}$ for 18 hours, and then dried for 3 hours at 50% R.H. at $25\text{ }^\circ\text{C}$ before detector assembly [20].

The detector assembly was performed at the CERN darkroom facility, with controlled environmental conditions (R.H. of 50% and temperature of $20\text{ }^\circ\text{C}$). The detector is organized in 73 modules, each consisting of 10 emulsion films and 10 tungsten plates, which were vacuum-packed with aluminum-laminated foils to isolate the detector from the external environment. Atmospheric pressure keeps the relative position of the different films within each module fixed during exposure.

¹The coordinate system associated to the FASER ν emulsion detector has the z -axis pointing along the LOS away from IP1, the y -axis pointing vertically upward, and the x -axis pointing horizontally toward the LHC machine. The origin of this coordinate system is aligned with the center of the emulsion detector in the transverse (x - y) plane and is located at the front of the emulsion detector along the z -axis.

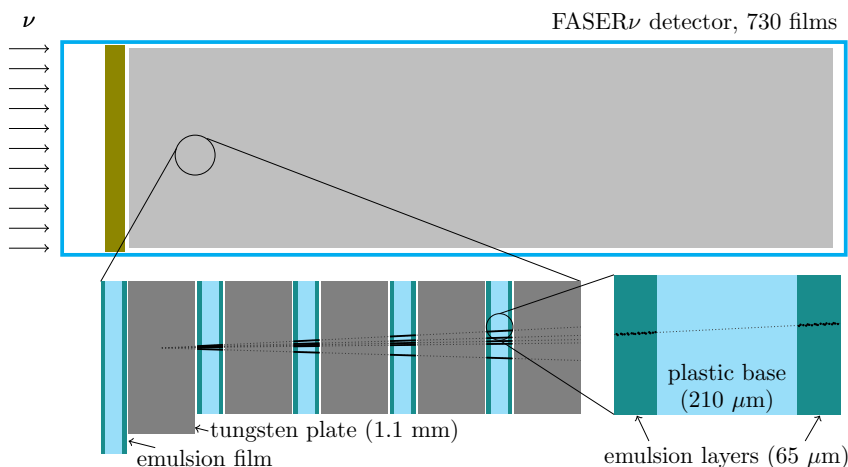


Figure 1. A schematic illustration of the FASER ν emulsion detector. The detector consists of a repeated structure of 730 layers, each composed of one tungsten plate and one emulsion film. The emulsion film is formed by a plastic base coated on both sides with emulsion layers.

All 73 modules are installed in a mechanical structure, which presses all modules to one side for optimal alignment. Since the emulsion detector records all charged particles, it must be periodically replaced. In fact, according to the expected muon background flux at FASER and taking into account that the maximum acceptable track density is 10^6 per cm^2 , the detector is replaced two or three times a year. Details of the detector and of the operational procedures are reported in ref. [4].

After installation, the emulsion detector is kept at a stable temperature of 16.5°C using a dedicated cooling system. The low temperature minimizes the increase in the number of random background silver grains per unit of emulsion area that develop without particle interaction (fog density). Furthermore, the temperature variation is also kept within $\pm 0.05^\circ\text{C}$ to avoid thermal expansion of the detector, which could affect the alignment of the emulsions in the FASER ν box.

After the exposure, the FASER ν detector is extracted, and the emulsion films undergo specific chemical development in the darkroom facility at CERN. This process amplifies the latent image stored in the silver bromide crystals by growing metallic silver filaments, forming visible dots that can be observed under optical microscopes. The amplification gain reaches approximately 10^8 , depending on the precise control of the temperature and development time [4].

The FASER ν analysis is based on the readout of the entire set of emulsion films by the Hyper Track Selector (HTS) system at Nagoya University [21]. During the scanning process, the films are placed on an acrylic plate and then scanned by the HTS, which is equipped with 72 2-mega-pixel high-speed cameras. It takes 22 tomographic images, and 16 successive images in the emulsion layer are used for track recognition. The system has a total data throughput of approximately 50 GBytes/s with 10 GBytes/s effectively used for the image readout. The data are distributed to 36 PCs with a total of 72 GPUs. The tomographic image data are processed, and track segments in a single emulsion layer, called micro-tracks, are reconstructed in real-time. Only micro-tracks are saved, while the raw data images are discarded. The angular acceptance for tracks is set to $\tan \theta < 1.5$, where θ is defined as the track angle to the normal vector to the film surface. The reconstruction of micro-tracks is limited by the computing power. While increasing the angular acceptance reduces the scanning speed, the system, in principle, has the potential to detect tracks with $\tan \theta \sim 4.0$.

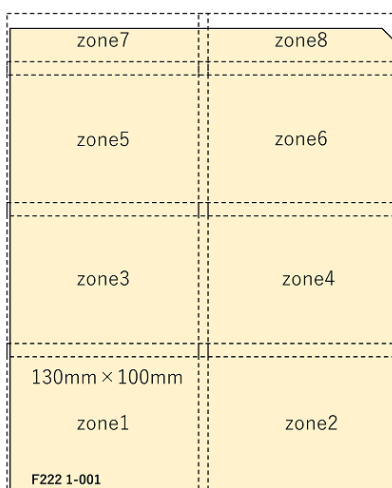


Figure 2. Definition of zones. The films are divided into eight zones for scanning. To determine the orientation of the films, a small triangular section (~ 5 mm) is cut at the top-right corner of each film during production.

The HTS scans a surface of $130\text{ mm} \times 100\text{ mm}$. Therefore, a $250\text{ mm} \times 300\text{ mm}$ film is divided into eight zones for scanning, as shown in figure 2. To ensure complete coverage, adjacent zones overlap by approximately 5 mm. It takes approximately 10 minutes to scan each zone, such that both sides of one film can be scanned in approximately 90 minutes, including the time to change the position of the film on the stage.

3 Reconstruction

This section details the event reconstruction process using the emulsion detector, as illustrated by the flowcharts in figure 3. For each scanned zone, track segments passing through the films, which are called base-tracks, are formed from the micro-tracks recorded within the emulsion layers. The reconstruction zone is divided into 63 areas, as shown in figure 4. Each area has a transverse size of $1.5\text{ cm} \times 1.5\text{ cm}$ including 1 mm overlap to ensure continuity between adjacent regions. Track and vertex reconstruction are performed for data units called sub-volumes, which contain one area across 30 consecutive plates. The sub-volumes start in plates 1, 11, 21, \dots , 701, so that the overlap of two consecutive sub-volumes in the longitudinal direction is 20 plates. Finally, for tracks near the neutrino vertex candidate, a follow-down method is applied to trace tracks across several (6 to 13, depending on the neutrino type) sub-volumes.

3.1 Base-track formation

The HTS system processes a set of 16 images for each emulsion layer to identify micro-tracks. These micro-tracks, however, include a significant number of fake tracks, which are due to randomly generated silver grains (fog). In addition, the positions and angles of the micro-tracks have large uncertainties due to the mechanical distortion of the emulsion layer.

As shown in figure 5, two micro-tracks, each belonging to the top and bottom layers of the film, are paired to form a base-track using their positions and angles. The base-track is reconstructed by

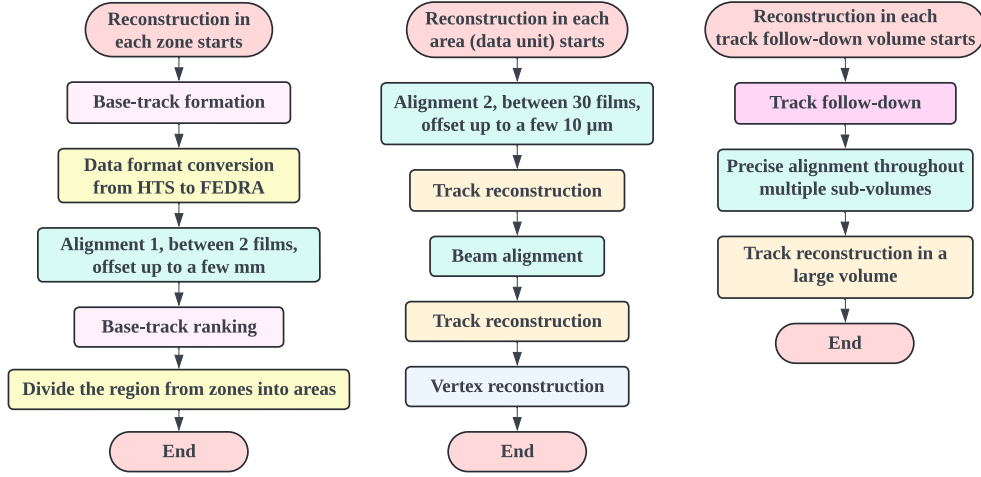


Figure 3. Flowcharts of the reconstruction processes.

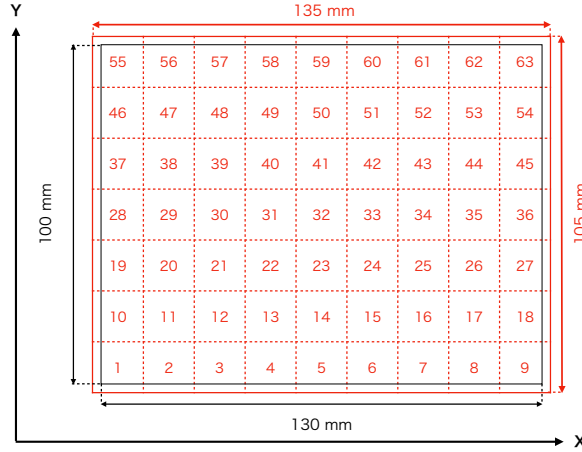


Figure 4. Division of a scanning zone into 63 overlapping areas, each with 1.7 cm × 1.7 cm size.

linking the endpoints of the micro-tracks at the emulsion-plastic base interface, thereby defining the trajectory on the plastic base. The angular measurement of the base-track becomes nearly independent of distortions in individual emulsion layers. Consequently, the angular resolution of the base-tracks is approximately ten times better than that of the micro-tracks.

Each track, either a micro-track or a base-track, is parameterised by four quantities: two position offsets (x, y) and two slopes ($\tan \theta_x, \tan \theta_y$) with respect to the z axis. The normalized residuals of the base-tracks Δ_{MT}^{BT} , calculated based on the angular deviations from the micro-tracks, is defined as

$$\Delta_{MT}^{BT} = \left\{ \left(\frac{\Theta_x^{MT, Top} - \Theta_x^{BT}}{\sigma(\Theta_{x,y}^{MT})} \right)^2 + \left(\frac{\Theta_y^{MT, Top} - \Theta_y^{BT}}{\sigma(\Theta_{x,y}^{MT})} \right)^2 + \left(\frac{\Theta_x^{MT, Bot} - \Theta_x^{BT}}{\sigma(\Theta_{x,y}^{MT})} \right)^2 + \left(\frac{\Theta_y^{MT, Bot} - \Theta_y^{BT}}{\sigma(\Theta_{x,y}^{MT})} \right)^2 \right\} / 2, \quad (3.1)$$

where $\tan \theta$ is written as Θ for simplicity. MT, BT denote micro-tracks and base-tracks, respectively. Top and Bot refer to the top and bottom of the emulsion layer, respectively. $\sigma(\Theta_{x,y}^{MT})$ is empirically

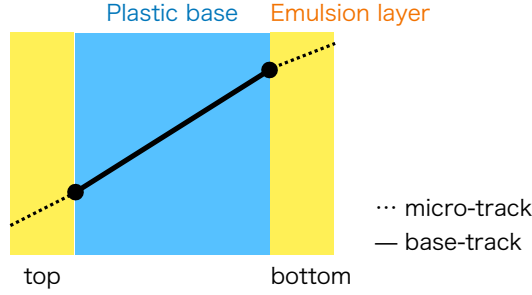


Figure 5. Base-tracks and micro-tracks. The solid lines represent base-tracks, reconstructed from the combinations of the micro-tracks, which are represented by dotted lines.

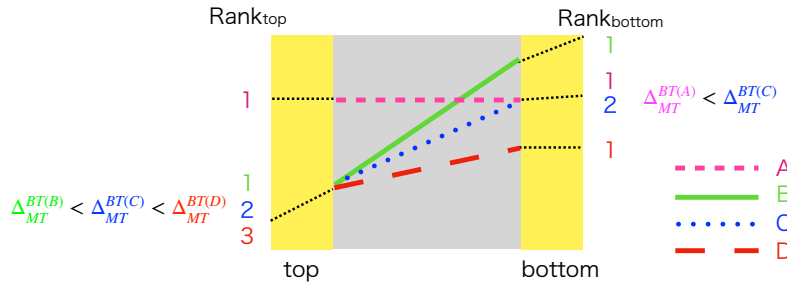


Figure 6. Base-track ranking algorithm. Base-track ranking algorithm is based on Δ_{MT}^{BT} (eq. (3.1)) when a micro-track connects to multiple base-tracks: the left-bottom micro-track is connected to the three base-tracks (B, C and D). The lower the value of the Δ_{MT}^{BT} , the higher will be the Rank_{top} value. The base-tracks with the condition of $\text{Rank}_{\text{top}} \leq 2$ and $\text{Rank}_{\text{bottom}} \leq 2$ are selected.

defined as $\sigma(\Theta_{x,y}^{MT}) = 0.008 \times \left(1 + 0.6 \times \sqrt{\theta_x^2 + \theta_y^2}\right)$, where θ_x and θ_y represent the angles of the micro-tracks in the x and y directions, respectively. The reconstruction requires that $\Delta_{MT}^{BT} < 15$ for the following reconstruction processes.

Due to the high concentration of tracks recorded in the detector, accidental coincidences of micro-tracks can also produce fake base-tracks. This is particularly problematic in the case of electromagnetic showers triggered by high-energy electrons and photons. This not only degrades the performance of the track reconstruction but also significantly increases the processing time of the track reconstruction. To reduce the number of fake base-tracks before the track reconstruction process, base-tracks formed from common micro-tracks are sorted in ascending order based on their Δ_{MT}^{BT} values, as illustrated in figure 6. Up to the best two base-tracks are kept based on this ranking. This criterion significantly reduces the computing time in the track reconstruction process, while maintaining a high base-track efficiency.

3.2 Alignment

Aligning the emulsion films, specifically placing base-tracks from different films within the same coordinate system, is a critical aspect of the FASER ν event reconstruction. Alignment is essential not only for track reconstruction but also for kinematic measurements, such as momentum assessment via multiple Coulomb scattering [6].

Base-track positions can be displaced for several reasons. The mechanical alignment precision of films within each vacuum pack is approximately 100 μm and, between vacuum packs, approximately 500 μm . The emulsion films are manually placed on an acrylic plate using guide lines for alignment. Subsequently, the film on the acrylic plate is mounted on the microscope, again manually aligned with the microscope's guide lines. The accuracy of human alignment of the film edge or corner to the reference position is typically on the order of a few hundred micrometres. In addition, the plastic base of the films is flexible and can be distorted during assembly, development, or placement on the microscope. Such distortions result in non-linear displacements that vary with position.

To compensate for these displacements, particle tracks are reconstructed in situ through several steps. The alignment parameters between two films are defined using an affine transformation and a gap in the z direction:

$$\begin{pmatrix} x_{2\text{ on }1} \\ y_{2\text{ on }1} \end{pmatrix} = \begin{pmatrix} a_{2\rightarrow 1} & b_{2\rightarrow 1} \\ c_{2\rightarrow 1} & d_{2\rightarrow 1} \end{pmatrix} \begin{pmatrix} x_2 \\ y_2 \end{pmatrix} + \begin{pmatrix} p_{2\rightarrow 1} \\ q_{2\rightarrow 1} \end{pmatrix}, \quad (3.2)$$

$$z_{2\text{ on }1} = z_2 + \Delta z_{2\rightarrow 1}. \quad (3.3)$$

Here, $a_{2\rightarrow 1}$, $b_{2\rightarrow 1}$, $c_{2\rightarrow 1}$, $d_{2\rightarrow 1}$, $p_{2\rightarrow 1}$, and $q_{2\rightarrow 1}$ are constants to be determined, representing translation, scaling, rotation, and shear parameters. "2 on 1" means that the coordinates of film 2 are transformed into those of the film 1 coordinate system. $\Delta z_{2\rightarrow 1}$ represents the adjustment in the z -coordinate from film 2 to film 1. This transformation adjusts the coordinates of film 2 to match those of film 1.

There are $O(10^5)$ muon tracks per cm^2 , which allow for highly precise alignment. The initial alignment between each pair of consecutive films is performed over a 13 cm \times 10 cm area using recorded base-tracks (alignment 1). However, since the emulsion films experience distortion at the $\sim 10 \mu\text{m}$ level across such a large area, a more refined alignment procedure is applied to smaller regions of 1.5 cm \times 1.5 cm (alignment 2), based on the FEDRA framework [15].

A critical issue of the film-to-film alignment is the accumulation of alignment errors over multiple films. This can cause straight particle tracks to be reconstructed as curved, as shown in the middle panel of figure 7. To address this, a further alignment is performed on the data-units with 30 plates. In this procedure, referred to as beam alignment, all films are aligned relative to the most upstream film, based on the assumption that high-energy muons travel along straight lines. This approach, depicted on the left side of figure 7, effectively corrects cumulative alignment errors. As a result, long-range tracks are reconstructed as straight, as shown in the right panel of the figure. The alignment precision is discussed in section 4.

3.3 Track reconstruction

After the first alignment procedure (alignment 1), base-tracks are connected across multiple plates to reconstruct the trajectories of charged particles. Note that base-track information is not discarded after track reconstruction, it is used for the following reconstruction processes and the kinematic measurements. To align the position displacement of the base-tracks in the localized area (alignment 2), the reconstruction volume is finely segmented before the track reconstruction process. The segmentation also reduces the computational memory needed for track reconstruction.

The algorithms for track reconstruction in emulsion detectors used so far are based on a matching test between two base-tracks. However, in case of a high track density, such as that expected at the LHC, these algorithms may fail because many tracks arrive at almost the same angle. Therefore, to

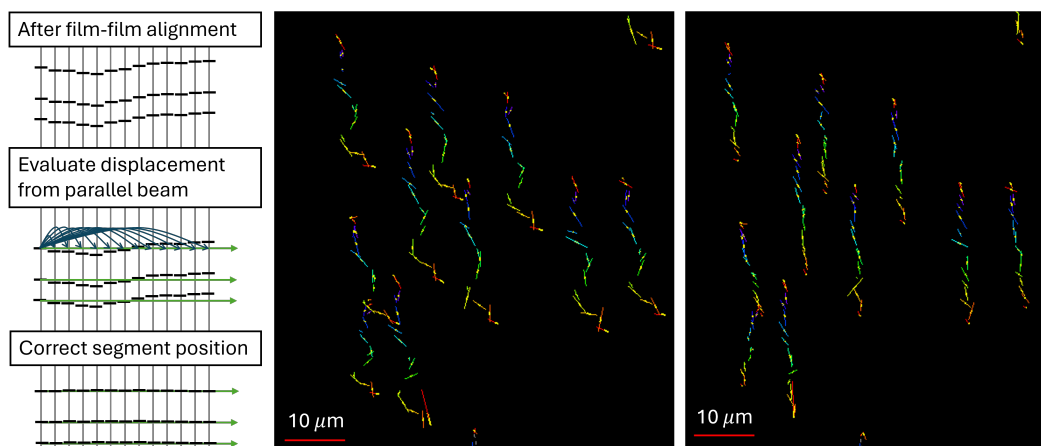


Figure 7. Alignment with a parallel particle beam. Left: a schematic of the beam-alignment procedure. Centre: reconstructed tracks in 15 films without the beam-alignment. Right: the same tracks with the beam-alignment. The centre and right figures are drawn in the X - Y plane of the emulsion detector, and the beam is nearly perpendicular to the plane.

cope with the expected very high track density, a new track reconstruction algorithm for emulsion detectors was developed for the NA65/DsTau experiment [18]. This algorithm, also adopted in FASER ν , allows for an improved track reconstruction extending the search for the track combinations across multiple plates. FASER ν also performs track reconstruction based on this improved algorithm, making reconstruction in high track density environments possible.

The track reconstruction process requires about 15 minutes per area for 30 plates, for a total data processing of approximately 1 hour per area, including the time for the alignment processes.

3.4 Vertex reconstruction

Vertex reconstruction is a crucial step in selecting candidate ν_e and ν_μ CC interactions since they form neutral vertices in FASER ν . Using the reconstructed tracks with $\tan \theta \leq 0.5$ passing through at least three plates, the minimum distances of all two-track combinations are calculated. If this distance is smaller than $3 \mu\text{m}$ and the opening angle of the two tracks is larger than 0.03 rad , additional tracks with an impact parameter to the vertex within $5 \mu\text{m}$ are searched for. Converging patterns with more than four tracks are selected as described in ref. [11]. Furthermore, converging patterns with more than two tracks are also selected and analysed by requesting an associated high-energy electromagnetic shower with reconstructed energy above 200 GeV to recover efficiency for the events with low track multiplicity. The procedure to define an electromagnetic shower is described in ref. [11]. If multiple vertex candidates are found within $20 \mu\text{m}$ in the x - y plane and $300 \mu\text{m}$ along the z direction, those with a lower track multiplicity are rejected. In the case they have the same track multiplicity, the downstream candidates are rejected. Tracks are then required to start within three films downstream of the vertices. Vertices are categorized as charged or neutral based on the presence or absence, respectively, of charged parent tracks. Hits in two more films are required to search for a parent track.

3.5 Track follow-down

The tracks reconstructed in individual sub-volumes, whose lengths do not exceed 30 plates, are used to search for vertices. For muon identification and further analysis, a follow-down process

for tracks (track follow-down, TFD) lying in the same area within ± 0.5 cm from the reconstructed vertex is performed. Thus, the maximum transverse dimension of the TFD volume is 1 cm^2 . Each TFD volume includes only those sub-volumes that are located one after the other sequentially in the longitudinal direction. It starts at least 10 plates upstream of the reconstructed vertex and ends at least 100 plates downstream. Tracks reconstructed in the data units are associated with one another, and those left by the same particles are connected from upstream to downstream. Since subsequent sub-volumes, which represent a unit of reconstruction in the beam direction, overlap in 20 plates, a track reconstructed in the upstream sub-volume can share up to 20 common segments with the corresponding track reconstructed in the next downstream sub-volume. Common segments are unambiguously distinguished by their identifiers, which are unique for each plate. Two tracks are then connected if they have at least six common segments. The efficiency of including individual base-tracks into reconstructed tracks obtained as final tracking results was verified to be independent of the selected value, ranging from six to ten common segments.

After two tracks from consecutive sub-volumes are associated to each other, segments of the track from the downstream sub-volume starting from the first non-common plate, are added to the corresponding track from the upstream sub-volume.

All the other tracks not connected from the downstream sub-volume are also added to the upstream sub-volume if they have more than one segment after the first non-common plate of the downstream sub-volume. Segments of such tracks are removed if they belong to one of the 20 common plates of the two overlapping sub-volumes. Part of these tracks can be connected with tracks from the downstream sub-volumes. Other, non-connected tracks are used in further analysis of neutrino event topologies, such as reconstruction of secondary hadron interactions or decay vertices.

After all analysed sub-volumes are connected, a more precise alignment (through multiple sub-volumes) is performed using tracks with a number of segments larger than 11. Segments from the first ten plates are used to estimate the track direction. The approximated x - z and y - z track slopes are used instead of individual track segment slopes for the alignment of consecutive plates. The obtained affine parameters, as well as the differences in the z positions, are used for the correction of all the track segments saved for further analysis. Finally, the tracking procedure is performed once again through all the connected sub-volumes by means of the aligned segments.

Figure 8 shows a typical event display with tracks reconstructed in a track follow-down volume and tracks associated with the reconstructed neutrino vertex. It demonstrates the ability to reconstruct a significant number of accumulated tracks and observe neutrino interactions.

4 Evaluation of detector performance

The performance of the FASER ν emulsion detector has been evaluated using data collected between July 26 and September 13, 2022, corresponding to 9.5 fb^{-1} of pp collisions at a centre-of-mass energy of 13.6 TeV. This dataset provides a comprehensive basis for assessing various detector characteristics including track reconstruction, single-film efficiency, and position and angular resolution. The results demonstrate that the detector performs as designed and is capable of achieving the required precision for neutrino interaction measurements [7]. The evaluation is supported by detailed simulations where neutrino interactions are modeled using GENIE [22, 23] while all the other interactions are simulated using GEANT4 [24]. These simulations incorporate realistic detector geometry and apply corrections to account for alignment and efficiency. Both simulation and experimental data are reconstructed

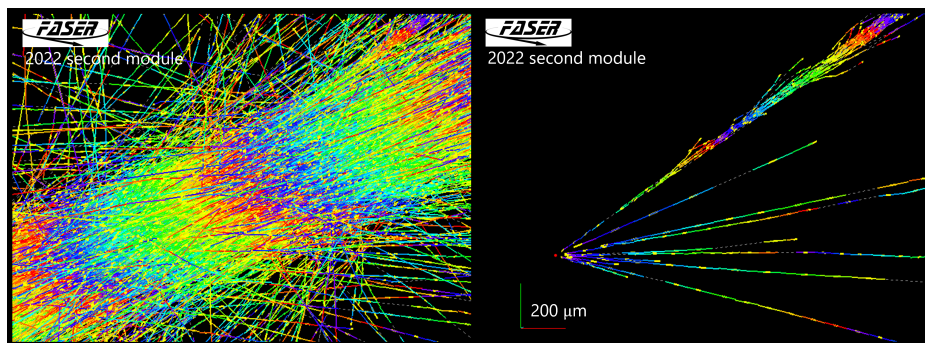


Figure 8. Example of event displays in the same 3D view showing all the reconstructed tracks in a region (left) and the reconstructed tracks associated with the neutrino vertex (right). In the right panel, the right-handed coordinate axes are shown in the bottom left, with blue, green, and red axes indicating the x (horizontal), y (vertical), and z (beam) directions, respectively. Yellow line segments show the trajectories of charged particles in the emulsion films. The other coloured lines are interpolations, with the colours indicating the longitudinal depth in the detector. The data corresponds to one of the electron neutrino events reported in ref. [11]. The displays show the same data region, demonstrating the ability to reconstruct a significant number of accumulated tracks and finally observe neutrino interactions. The longest track shown is going through 82 plates.

using the same method for a consistent comparison. The following subsections detail specific aspects of the detector performance evaluation.

4.1 Track density

The FASER ν emulsion detector, due to its intrinsic lack of time information, records all charged particles passing through it. Muons from the LHC collisions provide the main contribution through the detector. Figure 9 shows the track density distribution reconstructed in the data-units from the detector plate 41 to 70. No efficiency correction is applied to the track density calculation. A high density of $O(10^5)$ tracks per cm^2 has been measured across the bulk of the films, excluding the edges. For a track density of this order of magnitude, the average distance between adjacent tracks is approximately $32 \mu\text{m}$. The observed track density has a weak dependency on the position.

4.2 Single-film efficiency

The single-film efficiency is used to check the quality of the films, selecting the regions to be used in the physics analysis, and determining the efficiency correction parameters for the Monte Carlo simulations. Figure 10 shows how the efficiency is assessed. It is calculated using tracks reconstructed with five plates centred on the plate of interest. The efficiency is defined as the fraction of such tracks which have hits (i.e. reconstructed base-tracks) in this plate. As shown in figure 11, an efficiency of more than 85% is observed across the bulk of the films, with the exception of the edges, where regions with efficiency below 80% are observed. Therefore these regions are excluded in the physics analysis. Typical track requirements on the reconstructed tracks used for neutrino reconstruction require three hits out of seven films, which leads to a tracking efficiency of approximately 99.5% for a single-film efficiency of 80%.

4.3 Position and angular resolution

The position accuracy of the emulsion detector is essential for both the kinematic analysis of neutrino interactions and the measurement of individual charged particle momenta. A position resolution of

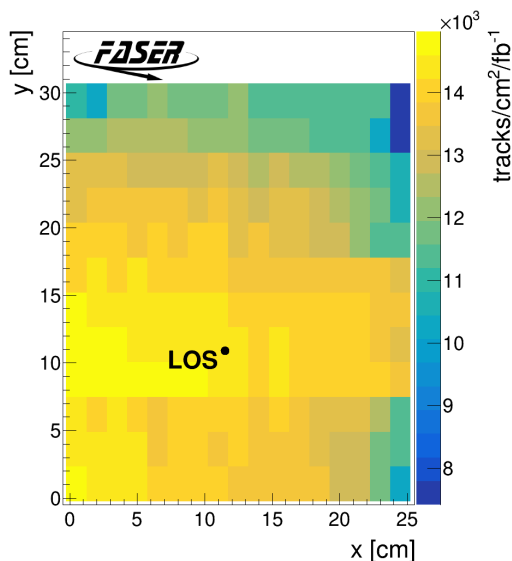


Figure 9. Track density map in the sub-volume from the detector plate 41 to 70. Tracks starting within the first five films and having more than five track segments and a track angle within 10 mrad from the angular peak are counted. Track angles are calculated by connecting the position of the first and the last segment of the tracks. The number of tracks is divided by 9.5 fb^{-1} . The line of sight (LOS) point represents the beam collision axis in the emulsion detector.

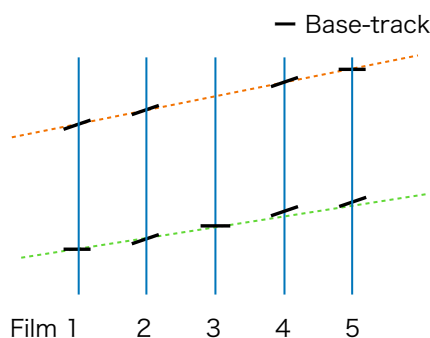


Figure 10. Patterns used for the calculation of a single-film efficiency. It is defined as the ratio of the number of tracks with hits recorded in the measured film (film 3) to the total number of tracks passing through it. Specifically, the denominator is the number of tracks with hits recorded in the two upstream and two downstream plates of the measured film (film 1, 2, 4, and 5). The numerator is the number of those tracks that also have hits recorded in the measured film.

$0.4 \mu\text{m}$ is required for measuring a momentum of 1 TeV based on the multiple Coulomb scattering method. The position resolution, or alignment precision, is evaluated using sets of five emulsion films. As shown schematically in figure 12 on the left, a straight line is fitted using the base-tracks on films 1, 2, 4, and 5, and the deviation of the base-track on film 3 from the fitted line is evaluated. As shown in figure 12 on the right, the typical position resolution is found to be $0.3 \mu\text{m}$. This value is consistent with the previously reported value for a data set with a $1.5 \text{ cm} \times 1.5 \text{ cm}$ size [18], and it can be improved by using a smaller processing size. figure 13 shows the position resolution as a

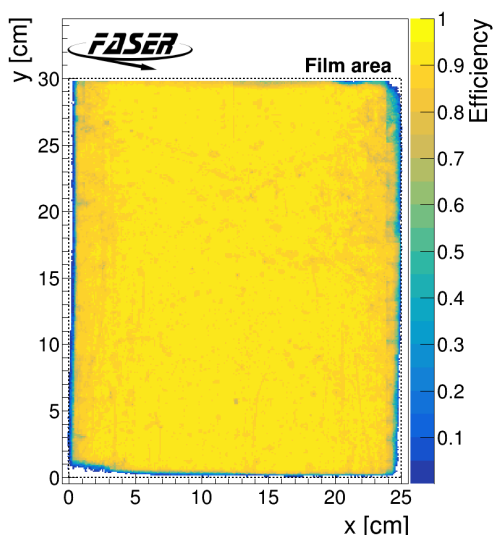


Figure 11. Distributions of the single-film efficiency for the sub-volumes consisting of plates from 41 to 70 of the detector.

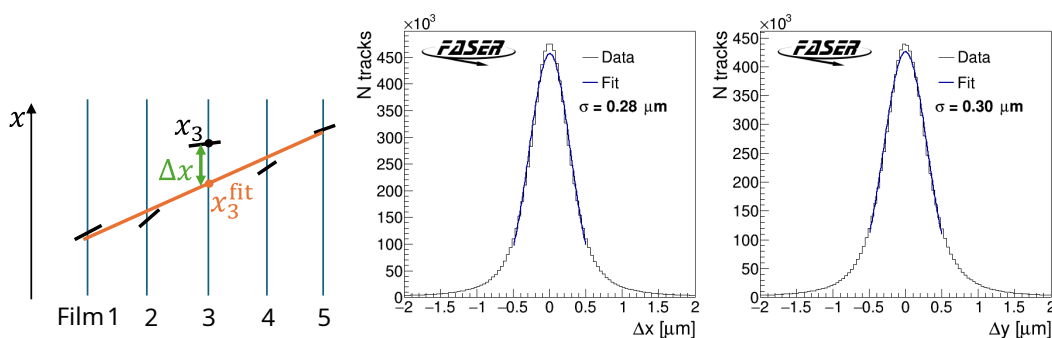


Figure 12. Evaluation of the alignment accuracy. Left: a schematic of the method. Centre and right: distributions of the position deviation of the base-tracks from the fitted line in a volume (plates 111 to 220) after the track follow-down processes. The distributions are obtained by combining data from multiple emulsion films, resulting in Gaussian-like residuals. Gaussian fittings (blue lines) give an alignment resolution of $0.3 \mu\text{m}$.

function of the plate number. Relatively poor resolution is observed in some plates, which is due to local distortion of the emulsion films.

Track angle measurement is a crucial component for both topological and kinematical analyses. The angles of leptons and hadrons, as well as their difference in the transverse plane with respect to the neutrino direction, $\Delta\phi$, are important variables for selecting neutrino events from neutral hadron backgrounds and determining the neutrino energy [11].

The angular resolution of the reconstructed tracks is evaluated by using background muons. The angular distribution of the muons has a spread of approximately $400 \mu\text{rad}$, corresponding to momenta above 1 TeV, considering the scattering in the 100 m of rock located in front of FASER ν . Track angles are determined from the position information of base-tracks within each set of 10 films in a track-follow-down volume. The analysis is based on the differences between the track angles measured in one 10-film volume and those in the subsequent volume. The angular difference between these two

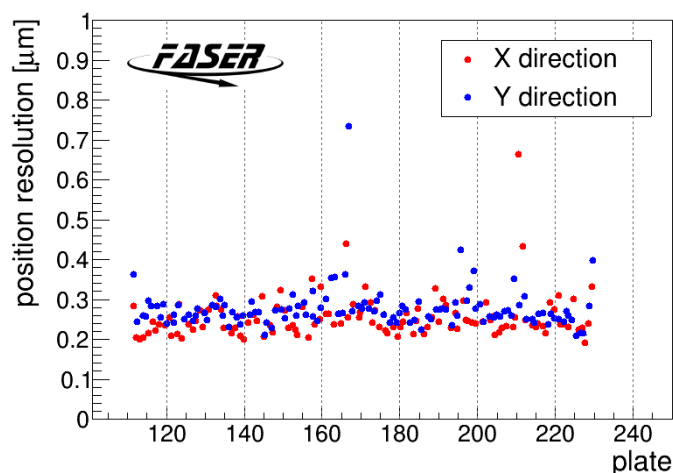


Figure 13. Position resolution as a function of plate number for one of the track follow-down volumes (plates 111 to 220).

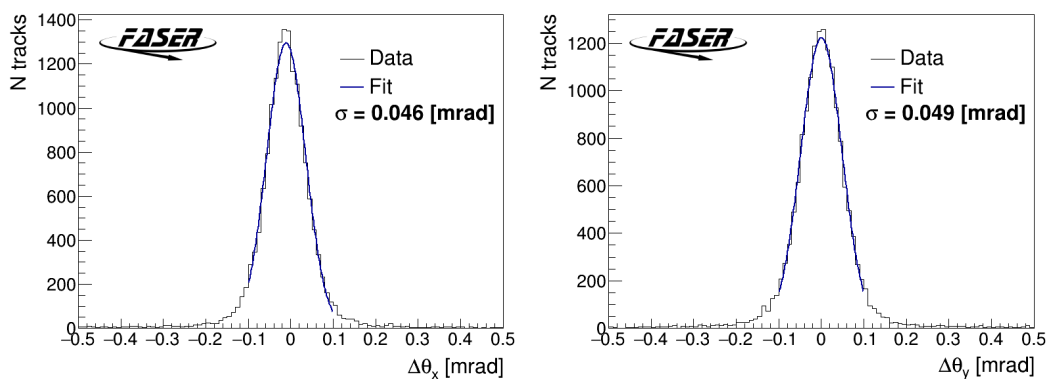


Figure 14. Angular resolution measured in data using high-energy muons with momenta of about 1 TeV. Tracks reconstructed over more than 20 films are used, and the angular difference between the first 10 films and the next 10 films is evaluated. The obtained angular deviations are $46 \mu\text{rad}$ and $49 \mu\text{rad}$, while the expected multiple Coulomb scattering angle for a 1 TeV muon is about $25 \mu\text{rad}$.

calculations is shown in figure 14. The Gaussian sigma of the resulting distribution was determined to be $46 \mu\text{rad}$ in the x -direction and $49 \mu\text{rad}$ in the y -direction.

4.4 Impact parameter

The impact parameter, defined as the minimum distance between the extrapolated track and the reconstructed vertex position, is a crucial quantity for evaluating the vertex reconstruction accuracy. A smaller impact parameter indicates better alignment between the tracks and the vertex, which is essential for identifying neutrino interaction events with high precision.

The vertex reconstruction algorithm discussed in section 3.4 reconstructs about 52% (45%) of ν_e (ν_μ) CC interactions. Out of the reconstructed neutral vertices in data, about 5% pass the neutrino event selection described in [11], while the remaining vertices are mainly due to neutral hadron interactions. Figure 15 shows the distribution of the impact parameter of the tracks forming the

vertices to the reconstructed vertex positions for the ν_μ CC signal events reported in ref. [11]. The agreement between the observed and simulated impact parameter distributions demonstrates the good performance of the vertex reconstruction algorithm. This comparison also serves as a validation of the simulation framework used for ν_μ CC signal modeling.

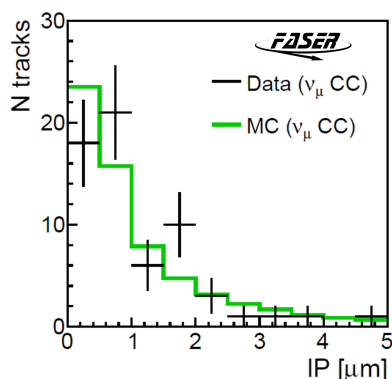


Figure 15. The distribution of the impact parameter of the tracks forming the vertices with respect to the reconstructed vertex positions for the observed ν_μ signal events reported in [11]. The observed ν_μ signal events from a 128.8 kg subset of the FASER ν volume, which collected 9.5 fb^{-1} of data, are shown in black. The distribution from Monte Carlo simulation is represented in green. The simulated distribution is normalized to the number of observed tracks.

5 Conclusion

This paper presents the event reconstruction techniques and performance evaluation of the FASER ν emulsion detector at the LHC, which achieves sub-micron precision in the reconstruction of charged particle tracks produced in the LHC collisions. The detector, constructed from 730 layers of tungsten and emulsion films, enables precise measurements of neutrino interactions. The challenges posed by high-density track environments, reaching $O(10^5)$ tracks per cm^2 , were addressed with advanced alignment techniques, dedicated track and vertex reconstruction algorithms, and a follow-down method for linking tracks across sub-volumes. Algorithms for track reconstruction at even higher densities are under development and are expected to be implemented in the future.

The data processing time for the described detector structure can be very roughly estimated for each zone as approximately one day/one plate/(one CPU + one GPU). In case of four processing servers with six processes running in parallel on each of them, it takes about seven months for full data processing of one FASER ν module.

The performance of the detector is evaluated in detail. More than 85% single-film efficiency is achieved across most regions of the emulsion films. The detector has an alignment precision of $0.3 \mu\text{m}$, which is sufficient for accurate momentum and kinematic studies. High track densities are successfully handled across the detector area, demonstrating the robustness of the system in a complex experimental environment. These results highlight the detector’s capability to identify neutrino interactions with exceptional spatial resolution and establish a solid base for future studies using the FASER ν emulsion detector.

Acknowledgments

We thank CERN for the excellent performance of the LHC and the technical and administrative staff members at all FASER institutions for their contributions to the success of the FASER experiment. We thank the ATLAS Collaboration for providing us with accurate luminosity estimates for the Run 3 LHC pp collision data. We also thank the CERN STI group for providing detailed FLUKA simulations of the muon fluence along the LOS, the CERN EN-HE group for their help with the installation/removal of the FASER ν detector, and the CERN EP department for the refurbishment of the CERN dark room, used for the preparation and development of the FASER ν emulsion. We thank Saya Yamamoto for supporting the preparation of emulsion films.

This work was supported in part by Heising-Simons Foundation Grant Nos. 2018-1135, 2019-1179, and 2020-1840, Simons Foundation Grant No. 623683, U.S. National Science Foundation Grant Nos. PHY-2111427, PHY-2110929, and PHY-2110648, JSPS KAKENHI Grant Nos. 19H01909, 22H01233, 20K23373, 23H00103, 20H01919, and 21H00082, the joint research program of the Institute of Materials and Systems for Sustainability, ERC Consolidator Grant No. 101002690, BMBF Grant No. 05H20PDRC1, DFG EXC 2121 Quantum Universe Grant No. 390833306, Royal Society Grant No. URF\R1\201519, U.K. Science and Technology Funding Councils Grant No. ST/T505870/1, the National Natural Science Foundation of China, Tsinghua University Initiative Scientific Research Program, and the Swiss National Science Foundation.

References

- [1] J.L. Feng, I. Galon, F. Kling and S. Trojanowski, *ForwArd Search ExpeRiment at the LHC*, *Phys. Rev. D* **97** (2018) 035001 [[arXiv:1708.09389](#)].
- [2] FASER collaboration, *Letter of Intent for FASER: ForwArd Search ExpeRiment at the LHC*, [arXiv:1811.10243](#).
- [3] FASER collaboration, *Technical Proposal for FASER: ForwArd Search ExpeRiment at the LHC*, [arXiv:1812.09139](#).
- [4] FASER collaboration, *The FASER detector*, *2024 JINST* **19** P05066 [[arXiv:2207.11427](#)].
- [5] L. Evans and P. Bryant, *LHC Machine*, *2008 JINST* **3** S08001.
- [6] FASER collaboration, *Detecting and Studying High-Energy Collider Neutrinos with FASER at the LHC*, *Eur. Phys. J. C* **80** (2020) 61 [[arXiv:1908.02310](#)].
- [7] FASER collaboration, *Technical Proposal: FASERnu*, [arXiv:2001.03073](#).
- [8] FASER collaboration, *First neutrino interaction candidates at the LHC*, *Phys. Rev. D* **104** (2021) L091101 [[arXiv:2105.06197](#)].
- [9] FASER collaboration, *First Direct Observation of Collider Neutrinos with FASER at the LHC*, *Phys. Rev. Lett.* **131** (2023) 031801 [[arXiv:2303.14185](#)].
- [10] FASER collaboration, *First Measurement of the Muon Neutrino Interaction Cross Section and Flux as a Function of Energy at the LHC with FASER*, *Phys. Rev. Lett.* **134** (2025) 211801 [[arXiv:2412.03186](#)].
- [11] FASER collaboration, *First Measurement of ν_e and ν_μ Interaction Cross Sections at the LHC with FASER's Emulsion Detector*, *Phys. Rev. Lett.* **133** (2024) 021802 [[arXiv:2403.12520](#)].
- [12] K. Kodama et al., *Detection and Analysis of Tau Neutrino Interactions in DONUT Emulsion Target*, *Nucl. Instrum. Meth. A* **493** (2002) 45.

- [13] DONuT collaboration, *Final tau-neutrino results from the DONuT experiment*, *Phys. Rev. D* **78** (2008) 052002 [[arXiv:0711.0728](#)].
- [14] CHORUS collaboration, *Final results on $\nu_\mu \rightarrow \nu_\tau$ oscillation from the CHORUS experiment*, *Nucl. Phys. B* **793** (2008) 326 [[arXiv:0710.3361](#)].
- [15] V. Tyukov, I. Kreslo, Y. Petukhov and G. Sirri, *The FEDRA Framework for emulsion data reconstruction and analysis in the OPERA experiment*, *Nucl. Instrum. Meth. A* **559** (2006) 103.
- [16] K. Hamada et al., *Comprehensive track reconstruction tool “NETSCAN 2.0” for the analysis of the OPERA Emulsion Cloud Chamber*, *2012 JINST* **7** P07001.
- [17] A. Ariga et al., *Nuclear Emulsions*, in *Particle Physics Reference Library. Volume 2: Detectors for Particles and Radiation*, C.W. Fabjan and H. Schopper eds., Springer (2020), p. 383–438 [[DOI:10.1007/978-3-030-35318-6_9](#)].
- [18] DsTAU collaboration, *DsTau: Study of tau neutrino production with 400 GeV protons from the CERN-SPS*, *JHEP* **01** (2020) 033 [[arXiv:1906.03487](#)].
- [19] H. Rokujo et al., *Nuclear emulsion film production system for experiments in full-area scanning and analysis era*, *Nucl. Instrum. Meth. A* **1066** (2024) 169622.
- [20] K. Ozaki et al., *Development of new-type nuclear emulsion for a balloon-borne emulsion gamma-ray telescope experiment*, *2015 JINST* **10** P12018.
- [21] M. Yoshimoto, T. Nakano, R. Komatani and H. Kawahara, *Hyper-track selector nuclear emulsion readout system aimed at scanning an area of one thousand square meters*, *PTEP* **2017** (2017) 103H01 [[arXiv:1704.06814](#)].
- [22] C. Andreopoulos et al., *The GENIE Neutrino Monte Carlo Generator*, *Nucl. Instrum. Meth. A* **614** (2010) 87 [[arXiv:0905.2517](#)].
- [23] C. Andreopoulos et al., *The GENIE Neutrino Monte Carlo Generator: Physics and User Manual*, [arXiv:1510.05494](#).
- [24] GEANT4 collaboration, *GEANT4 — A Simulation Toolkit*, *Nucl. Instrum. Meth. A* **506** (2003) 250.

The FASER collaboration

Roshan Mammen Abraham ¹, Xiaocong Ai ², Saul Alonso Monsalve ³, John Anders ⁴, Claire Antel ⁵, Akitaka Ariga ^{6,7}, Tomoko Ariga ⁸, Jeremy Atkinson ⁶, Florian U. Bernlochner ⁹, Tobias Boeckh ⁹, Jamie Boyd ⁴, Lydia Brenner ¹⁰, Angela Burger ⁴, Franck Cadoux⁵, Roberto Cardella ⁵, David W. Casper ¹, Charlotte Cavanagh ¹¹, Xin Chen ¹², Kohei Chinone ⁷, Dhruv Chouhan ⁹, Andrea Coccaro ¹³, Stephane Débieux⁵, Ansh Desai ¹⁴, Sergey Dmitrievsky ^{15,*}, Radu Dobre ¹⁶, Monica D’Onofrio ¹⁷, Sinead Eley ¹⁷, Yannick Favre⁵, Deion Fellers ¹⁴, Jonathan L. Feng ¹, Carlo Alberto Fenoglio ⁵, Didier Ferrere ⁵, Max Fieg ¹, Wissal Filali ⁹, Elena Firu ⁹, Haruhi Fujimori ⁷, Edward Galantay ^{4,5}, Ali Garabaglu ¹⁸, Stephen Gibson ¹⁹, Sergio Gonzalez-Sevilla ⁵, Yuri Gornushkin ¹⁵, Carl Gwilliam ¹⁷, Daiki Hayakawa ^{7,*}, Michael Holzbock ⁴, Shih-Chieh Hsu ¹⁸, Zhen Hu ¹², Giuseppe Iacobucci ⁵, Tomohiro Inada ⁸, Luca Iodice ⁵, Sune Jakobsen ⁴, Hans Joos ^{4,20}, Enrique Kajomovitz ²¹, Takumi Kanai ⁷, Hiroaki Kawahara ⁸, Alex Keyken ¹⁹, Felix Kling ²², Daniela Köck ¹⁴, Pantelis Kontaxakis ⁵, Umut Kose ¹¹, Rafaella Kotitsa ⁴, Peter Krack ¹⁰, Susanne Kuehn ⁴, Thanushan Kugathanan ⁵, Lorne Levinson ²³, Botao Li ³, Jinfeng Liu ¹², Yi Liu ², Margaret S. Lutz ⁴, Jack MacDonald ²⁴, Chiara Magliocca ⁵, Toni Mäkelä ¹, Lawson McCoy ¹, Josh McFayden ²⁵, Andrea Pizarro Medina ⁵, Matteo Milanesio ⁵, Théo Moretti ⁵, Keiko Moriyama ⁸, Mitsuhiro Nakamura ²⁶, Toshiyuki Nakano ²⁶, Laurie Nevay ⁴, Motoya Nonaka ⁷, Yuma Ohara ⁷, Ken Ohashi ⁶, Kazuaki Okui ⁷, Hidetoshi Otono ⁸, Hao Pang ¹², Lorenzo Paolozzi ^{5,4}, Pawan Pawan ¹⁷, Brian Petersen ⁴, Titi Preda ¹⁶, Markus Prim ⁹, Michaela Queitsch-Maitland ²⁷, Juan Rojo ¹⁰, Hiroki Rokujo ⁸, André Rubbia ¹¹, Jorge Sabater-Iglesias ⁵, Osamu Sato ²⁶, Paola Scampoli ^{6,28}, Kristof Schmieden ⁹, Matthias Schott ⁹, Christiano Sebastiani ⁴, Anna Sfyrla ⁵, Davide Sgalaberna ¹¹, Mansooraa Shamim ⁴, Savannah Shively ¹, Yosuke Takubo ²⁹, Noshin Tarannum ⁵, Ondrej Theiner ⁵, Simon Thor ³, Eric Torrence ¹⁴, Oscar Ivan Valdes Martinez ²⁷, Svetlana Vasina ¹⁵, Benedikt Vormwald ⁴, Yuxiao Wang ¹², Eli Welch ¹, Monika Wielers ³⁰, Benjamin James Wilson ²⁷, Jialin Wu ³, Johannes Martin Wuthrich ³, Yue Xu ¹⁸, Stefano Zambito ⁵, Shunliang Zhang ¹², and Xingyu Zhao ³

¹ Department of Physics and Astronomy, University of California, Irvine, CA 92697-4575, U.S.A.

² School of Physics, Zhengzhou University, Zhengzhou 450001, China

³ ETH Zurich, 8092 Zurich, Switzerland

⁴ CERN, CH-1211 Geneva 23, Switzerland

⁵ Département de Physique Nucléaire et Corpusculaire, University of Geneva, CH-1211 Geneva 4, Switzerland

⁶ Albert Einstein Center for Fundamental Physics, Laboratory for High Energy Physics, University of Bern, Sidlerstrasse 5, CH-3012 Bern, Switzerland

⁷ Department of Physics, Chiba University, 1-33 Yayoi-cho Inage-ku, 263-8522 Chiba, Japan

⁸ Kyushu University, 744 Motoooka, Nishi-ku, 819-0395 Fukuoka, Japan

⁹ Universität Bonn, Regina-Pacis-Weg 3, D-53113 Bonn, Germany

¹⁰ Nikhef National Institute for Subatomic Physics, Science Park 105, 1098 XG Amsterdam, Netherlands

¹¹ Institute for Particle Physics, ETH Zürich, Zürich 8093, Switzerland

¹² Department of Physics, Tsinghua University, Beijing, China

¹³ INFN Sezione di Genova, Via Dodecaneso, 33-16146, Genova, Italy

¹⁴ University of Oregon, Eugene, OR 97403, U.S.A.

¹⁵ Affiliated with an international laboratory covered by a cooperation agreement with CERN.

¹⁶ Institute of Space Science — INFLPR Subsidiary, Bucharest, Romania

¹⁷ University of Liverpool, Liverpool L69 3BX, United Kingdom

¹⁸ Department of Physics, University of Washington, PO Box 351560, Seattle, WA 98195-1460, U.S.A.

¹⁹ Royal Holloway, University of London, Egham, TW20 0EX, United Kingdom

- ²⁰ *II. Physikalisches Institut, Universität Göttingen, Göttingen, Germany*
- ²¹ *Department of Physics and Astronomy, Technion — Israel Institute of Technology, Haifa 32000, Israel*
- ²² *Deutsches Elektronen-Synchrotron DESY, Notkestr. 85, 22607 Hamburg, Germany*
- ²³ *Department of Particle Physics and Astrophysics, Weizmann Institute of Science, Rehovot 76100, Israel*
- ²⁴ *Institut für Physik, Universität Mainz, Mainz, Germany*
- ²⁵ *Department of Physics & Astronomy, University of Sussex, Sussex House, Falmer, Brighton, BN1 9RH, United Kingdom*
- ²⁶ *Nagoya University, Furo-cho, Chikusa-ku, Nagoya 464-8602, Japan*
- ²⁷ *University of Manchester, School of Physics and Astronomy, Schuster Building, Oxford Rd, Manchester M13 9PL, United Kingdom*
- ²⁸ *Dipartimento di Fisica “Ettore Pancini”, Università di Napoli Federico II, Complesso Universitario di Monte S. Angelo, I-80126 Napoli, Italy*
- ²⁹ *National Institute of Technology (KOSEN), Niihama College, 7-1, Yakumo-cho Niihama, 792-0805 Ehime, Japan*
- ³⁰ *Particle Physics Department, STFC Rutherford Appleton Laboratory, Harwell Campus, Didcot, OX11 0QX, United Kingdom*

* *Corresponding author*